Generation and Characterization of Phase-Stable Sub-Single-Cycle Pulses at 3000 cm^{-1}

Takao Fuji, Yutaka Nomura, and Hideto Shirai

(Invited Paper)

Abstract—This paper summarizes the generation of sub-single-cycle infrared (IR) pulses through a laser filament and the detailed properties of the generated pulses. The fundamental (ω_1) and second harmonic (ω_2) of 30-fs Ti:sapphire amplifier output were focused into nitrogen gas and produced phase-stable broadband IR pulses (ω_0) by four-wave difference frequency generation ($\omega_1 + \omega_1 - \omega_2 \rightarrow \omega_0$) through filamentation. The spectrum spread from 200 to 5500 cm^{-1}, corresponding to ~3.5 octaves. The waveform of the sub-single-cycle pulse was completely characterized with the frequency-resolved optical gating capable of a carrier-envelope phase determination. The pulse duration was measured as 6.9 fs, which was 0.63 times the period of the carrier frequency, 3000 cm^{-1}. The carrier-envelope phase of the IR pulse was passively stabilized, and the instability of the phase was estimated as 154-mrad rms over 2.5 h. We also summarize a particular behavior of the spectral phase of the sub-single-cycle pulse; the phase of high-frequency components of the generated pulses changes continuously and linearly with the relative phase between the two-color input pulses, whereas the phase of the low-frequency components takes only two discrete values. The phase behavior is a unique feature of single-cycle pulses generated with a passive carrier-envelope phase stabilization scheme.

Index Terms—Filamentation, infrared, ultrashort pulse, four-wave difference frequency generation, single-cycle pulse.

I. INTRODUCTION

GENERATION of carrier-envelope phase (CEP)-stable single-cycle pulses is a key technology for ultrafast science. The well-defined oscillation of the electric field can be used for investigation of attosecond dynamics in atoms, molecules and solids. One of the most important applications of the single-cycle pulses would be generation of isolated attosecond pulses.

So far several types of single-cycle pulse generation schemes have been experimentally demonstrated. One is the generation and synthesis of several discrete harmonics spanning over two octaves from a quasi-monochromatic light source. Single-cycle or sub-single-cycle pulse trains with the period of several femtoseconds have been successfully generated by using such schemes [1]–[3].

Another is based on the coherent synthesis of a few multi-color phase-stable femtosecond pulses. In this way, isolated single-cycle pulses are generated. The method has been demonstrated by several groups [4]–[6], and generation of isolated attosecond pulses with the multi-color femtosecond pulses has also been successful [7], [8].

Terahertz (THz) wave generation through optical rectification should be counted as a method to generate CEP-stable single-cycle pulses. Single-cycle pulses have been rather easily generated with the process since the period of the center frequency (~sub-picoseconds) is much longer than that of visible pulses (~femtoseconds). By analogy to the passive stabilization of the CEP through difference frequency generation [9], [10], the CEP of the THz pulse generated through optical rectification is usually stable even when the CEP of the input pulse for the frequency conversion is not stable. In particular, four-wave rectification in gases [11] is effective for generation of broadband and single-cycle pulses [12], [13].

In 2007, Fuji and Suzuki applied the four-wave rectification scheme for generation of mid-infrared (IR) pulses. They succeeded in generation of 1.3-cycle mid-IR pulses by using four-wave rectification through filamentation in gases [14]. Due to the cross-phase modulation enhanced through the filamentation, the central frequency of the generated pulse becomes much higher than THz and the highest frequency components reach close to the near-IR region (~5000 cm^{-1}). The technology has been further developed by several groups [15]–[19], and used for advanced IR spectroscopy [20]–[23]. Currently, the bandwidth spread from far- to near-IR region, and 7-fs pulses with the central frequency of 3000 cm^{-1} are generated by using the scheme [24]. The number of cycles is 0.63, which is well below single-cycle or even nearly half-cycle pulse.

Fig. 1 summarizes the bandwidths of the single-cycle pulses reported so far. Since the frequency axis is written in a logarithmic scale, the length of the bar in the figure is basically proportional to the number of octaves, or the inverse of the cycle number. The length of the bar tends to become longer in the lower frequency region. It is rather natural that the number of cycles becomes fewer in the lower frequency region since the necessary bandwidth for one octave is narrower. Sub-single-cycle pulses have basically been generated in the IR region (<10000 cm^{-1}). In addition to the fewer cycle numbers, IR pulses have several benefits for high field physics. As was written in the previous paragraphs, the passive CEP stabilization scheme is easily implemented for generation of sub-single-cycle IR pulses. Moreover, a lower frequency driver laser pulse would
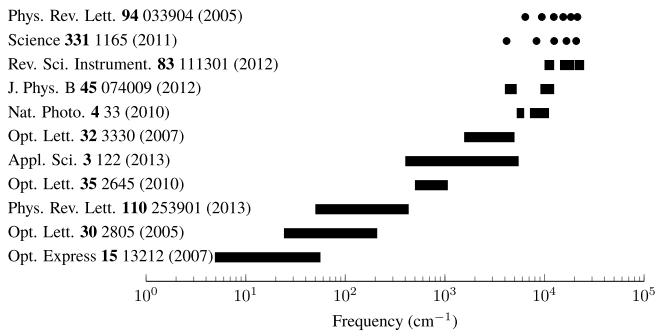
Fig. 1. Bandwidths of the single-cycle pulses (<1.5-cycle pulses) reported so far. Each reference shows on the side of each bar. The full width at tenth maximum of the bandwidth for each pulse is shown. For the spectrum which consists of discrete frequency lines, we show each frequency line as a closed circle.

be suitable to generate higher photon-energy high harmonics due to the pondermotive energy scaling with the square of wavelength [25]. It may result in shorter attosecond pulse generation via high harmonic generation. Recently, the scaling of the harmonic cutoff was clearly demonstrated with high energy mid-IR pulses [26].

From the above discussion, it is understandable that the detail of the sub-single-cycle pulse generation scheme based on four-wave rectification is worth to discuss for attosecond science community although the intensity of the sub-single-cycle pulse generated by using the scheme is still not enough to generate extreme ultraviolet attosecond pulses.

In this review, we summarize the detail of the performance of the IR pulses generated by using four-wave rectification through filamentation. The fundamental (ω_1) and second harmonic (SH, ω_2) pulses from a 30-fs Ti:sapphire amplifier were focused into nitrogen gas and phase-stable broadband IR (ω_0) pulses were produced through four-wave rectification process ($\omega_1 + \omega_1 - \omega_2 \rightarrow \omega_0$). We also summarize the full characterization of the sub-single-cycle pulse by using frequency-resolved optical gating capable of carrier-envelope phase (FROG-CEP) determination [27], [28].

The paper is organized as follows: Section II introduces the generation scheme of the ultrabroadband IR pulses and the fundamental properties, such as spectrum, beam profile, and CEP stability. In Section III we discuss the waveform characterization of the sub-single-cycle pulse. Section IV shows the CEP control of the sub-single-cycle pulse. The paper concludes by outlining current and future applications of the light source.

II. Ultrabroadband IR Pulse Generation

A. Experimental Setup

The experimental setup for the ultrabroadband IR pulse generation is shown in Fig. 2(a). The light source was based on a Ti:sapphire multi-pass amplifier system (790 nm, 30 fs, 0.85 mJ at 1 kHz, Femtopower compactPro, FEMTOLASERS) with a Dazzler (Fastlite) stretcher and a transmission grating compressor. In the previous experiment, we were using a system based on

a prism compressor [17]. The transmission grating compressor significantly improves the temporal and spatial beam profiles, and it results in improvement of the quality of the generated IR pulses. A delay plate and a dual wave plate were inserted in the path of the co-propagating fundamental and SH pulses, and used to adjust the delay and the polarization of the fundamental and SH pulses inline [16], [20], [29], [30]. SH (ω_2, 15 μJ) was generated through Type-I frequency doubling by sending the collimated fundamental beam into a 0.1 mm thick BBO crystal cut at 29°. It was easy to achieve more than 10% efficiency of the second harmonic generation (SHG). However, we tilted the crystal from the optimal angle for two reasons. One is to reduce the conversion efficiency to avoid back conversion effects that distort the fundamental beam profile, and the other is to generate SH at slightly longer wavelengths, which helps to generate a broad IR spectrum. Temporal walkoff in the doubling crystal and wave plate was compensated by a delay plate, which was a 1.7-mm-thick calcite crystal. A dual wave plate (λ at 400 nm and $\lambda/2$ at 800 nm) was used to adjust the relative polarizations of the fundamental and SH pulses. The beam was focused into nitrogen at around atmospheric pressure by a concave mirror ($r = 1$ m), and a bright filament was generated with a length of ~3.5 cm around the beam focus as is shown in Fig. 2(b). It is about ten times longer than the confocal parameter of the fundamental beam estimated by Gaussian beam optics. Ultrabroadband IR pulses (ω_0) were generated by four-wave difference frequency generation (FWDFG) ($\omega_1 + \omega_1 - \omega_2 \rightarrow \omega_0$). The energy of this IR pulse was measured as ~0.5 μJ by using a pyroelectric detector (J-10MB-LE, Coherent). The pulse-to-pulse intensity fluctuation was about 1.6% rms while that of the amplifier output was about 1.0% rms. The reason for the smaller fluctuation than the simple estimation, three times less than the input pulse instability, would be caused by the saturation of FWDFG [31] and/or intensity clamping effect of filamentation [32], [33].

B. Spectra

Spectra of the fundamental and SH used for the IR generation are shown in Fig. 3(a) and (b). Both the fundamental and SH spectra showed significant ionization-induced blue shift. The broadening of the SH spectrum is due to cross-phase modulation between the fundamental and SH pulses since the broadening of the SH spectrum only occurs when the delay between the fundamental and SH pulses is adjusted. The fundamental pulse was self-compressed down to 15 fs, which was characterized with cross-correlation frequency-resolved optical gating (XFROG) [35]. The FROG error was 0.76%.

The spectrum of the IR pulse could be in principle obtained by using a Fourier transform spectrometer. However, it is not essentially possible to measure the frequency range from far- to near-IR at once since there is no beam splitter which works for such a broadband spectral range. Here, we used a chirped-pulse upconversion scheme to measure the spectrum [21], [36]. The schematic of the measurement system is shown in the right-hand-side of Fig. 2(a). A portion of the fundamental pulse (~0.1 mJ, ω_1) was stretched to 4.9 ps by passing through two
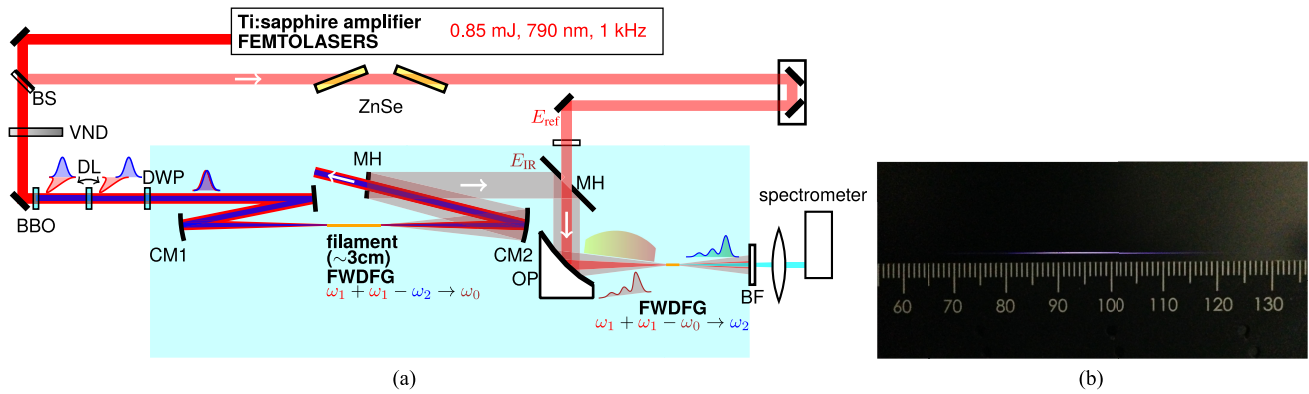
Fig. 2. (a) Schematic of the system for generation and chirped-pulse upconversion of sub-single-cycle pulses. Shaded region was purged with nitrogen at around atmospheric pressure. BS: beam splitter (15% reflection), VND: variable neutral density filter, BBO: β-BaB$_2$O$_4$ crystal (Type 1, $\theta = 29°$, $t = 100$ μm), DL: delay plate (calcite crystal, $t = 1.7$ mm), DWP: dual wave plate (λ at 400 nm, $\lambda/2$ at 800 nm), ZnSe: zinc selenide substrate ($t = 10$ mm), CM1: $r = 1$ m concave mirror, CM2: $r = 0.5$ m concave mirror, MH: aluminium-coated mirror with a hole ($\phi = 7$ mm). OP: aluminium-coated off-axis parabolic mirror, BF: blue filter (FGB37, Thorlabs), (b) Picture of the filament created by focusing fundamental and SH of the Ti:sapphire amplifier output in nitrogen gas.
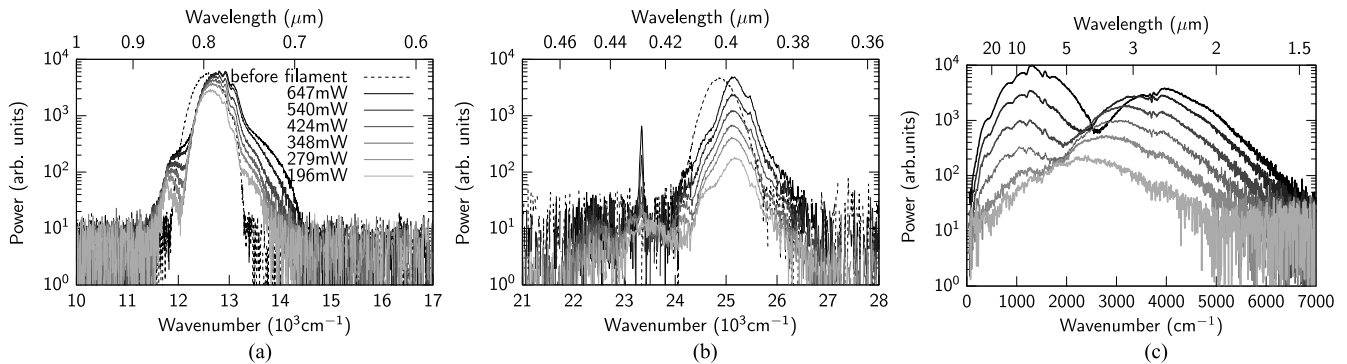

Fig. 3. (a) Fundamental spectra measured before and after the filament (dotted and solid curves, respectively). Each input power in front of the BBO crystal is shown. (b) SH spectra measured before and after the filament (dotted and solid curves, respectively). Each input power in front of the BBO crystal is shown in (a). A sharp structure at 428 nm is a lasing line due to the filamentation [34]. (c) Spectra of the IR pulse at various input powers. The spectra were recorded by using the chirped pulse upconversion scheme. Each input power for each IR spectrum is shown in (a).

zinc selenide crystals ($t = 10$ mm) with a Brewster angle, which corresponds to the group delay dispersion of $\sim$22 000 fs^2. The chirped pulse was overlapped with the IR pulse (ω_0) and tightly focused by using an off-axis parabola ($f = 50$ mm) into nitrogen gas. We recorded the upconversion signal (ω_2) generated by FWDFG, $\omega_1 + \omega_1 - \omega_0 \rightarrow \omega_2$. The spectrum of the FWDFG signal spread over from 400 to 500 nm. Since the bandwidth of the phase matching of the FWDFG is extremely wide due to the low dispersion of the nonlinear medium, nitrogen gas, the whole bandwidth of the IR pulse was converted into visible. The spectrum was recorded with a visible spectrometer which consisted of an imaging spectrograph and an EMCCD camera (SP-2358 and ProEM+1600, Princeton Instruments). The IR spectrum can be retrieved from the upconversion spectrum by using a simple algorithm based on Fourier-transform [37].

The broadband spectrum spread over the whole IR region (400–5500 cm^{-1} at tenth maximum). We recorded the input intensity dependence of the spectrum. We changed the intensity of the input beam by using a variable neutral density filter as is shown in Fig. 2(a). The spectra of fundamental, SH, and IR pulses are shown in Fig. 3. The IR spectrum becomes significantly broad by increasing the intensity of the input pulses

although the bandwidths of the input pulses do not become so broad. This means that the broadness of the spectrum comes not only from the weak dispersion of the medium but also from the cross-phase modulation between the fundamental and IR pulses.

Here we discuss the differences between the IR generation and the THz generation experiments. The first point is the length of the plasma. At the THz generation, typical length of the plasma is about 5 mm, which is seven times shorter than our experiment. Considering the confocal parameter of THz wave and mid-IR wave, it is understandable that longer length of plasma does not contribute very much to increase the efficiency of the THz generation but contribute to increase the shorter wavelength components, namely mid-IR components here. The second point is the adjustment of the relative delay and polarization of the input pulses. At the THz generation experiments in the references [11], [13], [19], [30], [38]–[46], only the angles of the BBO crystal for the SHG can be adjusted to optimize the efficiency of the wavelength conversion. In this case, the freedom to control the relative delay and polarizations of the fundamental and SH pulses is seriously limited. In contrast, by using the inline scheme with a delay plate and a dual wave plate, it is possible to perfectly adjust the relative delay and polarizations
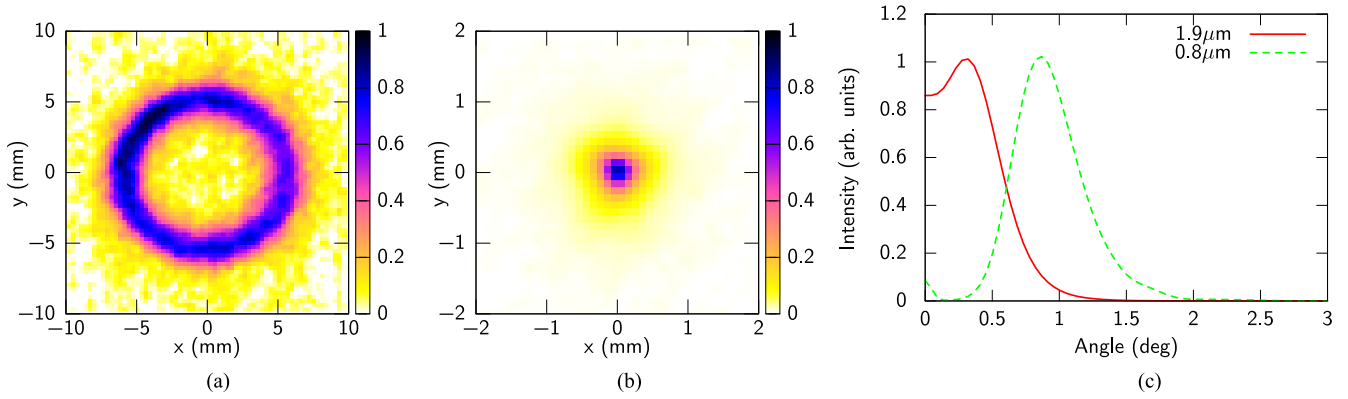
Fig. 4.   (a) Experimental radial intensity distribution 250 mm after the generation point (on CM2 in Fig. 2(a)) of the IR pulses. (b) The intensity distribution at the focal point of the IR pulse focused with a concave mirror ($r = 2$ m). (c) The intensity distribution of the IR signal as a function of the angle from the propagation axis. The solid and dotted curves show the IR intensities with 1.9 μm and 0.8 μm pump wavelength, respectively.

of the fundamental and SH pulses. The adjustment of the two input pulses affects not only the efficiency of the wavelength conversion but also that of the cross-phase modulation among the multi-color waves. As is discussed in the previous paragraphs, the cross-phase modulation is a key process to generate short wavelengths. The third point is the detection scheme for the generated pulses. In the above mentioned references, only electro-optic sampling (EOS) was used to detect the generated pulses. However, the frequency detectable with EOS is limited by the duration of the reference pulse [47]. For example, reference pulses as short as 5 fs are necessary to detect a mid-IR wave at 3 μm in reasonable accuracy. Such short pulses were never used in the above mentioned references. In such situations, even they generated IR components, it is not possible to detect them.

C. Beam Profile

The beam profile of the single-cycle pulse after a Ge ($t = 0.5$ mm) filter measured with a pyroelectric camera (Pyrocam III, Spiricon) is shown in Fig. 4(a). The shape of the beam was a ring and the angle of the cone was estimated to be about 3°. The cone angle of the beam can be explained by phase matching condition [48], [49].

The generated IR pulse has basically pure one-direction linear polarization (>40:1) in the entire cross-section of the beam as the input pulses, which was confirmed with a wire grid polarizer (NT62-774, Edmund Optics).

The ~12 mm diameter beam was focused down to 0.9 mm (at $1/e^2$) with a concave mirror ($r = 2$ m), indicating a reasonable focusability for a ring-shaped spatial mode. The beam profile at the focal point is shown in Fig. 4(b).

Similar conical emission was also observed for mid-IR or THz pulse generation from two-color air plasma [18], [46], [50].

This beam profile is obviously unsuitable for the study of high field physics. However, if we can provide longer wavelength pump beam, the beam profile should be improved. We did a simple calculation based on a standard equation for the radial intensity profile of the signal $I_4(r)$ resulting from the

$\omega_1 + \omega_1 - \omega_2 \rightarrow \omega_0$ FWDFG process [48]:

$$I_4(r) \sim \left| \int_{-\zeta}^{\epsilon} d\epsilon' \frac{\exp\left[-(ib/2)\Delta k(\epsilon' - \epsilon)\right]}{(1 + i\epsilon')(k'' - ik'\epsilon')H} \right|^2 \quad (1)$$

where r is the radial coordinate transverse to the direction of beam propagation axis z, $\epsilon = 2(z - f)/b$, $\zeta = 2f/b$, b is the confocal parameter, f is the focal length, $k' = 2k_1 - k_2$, $k'' = 2k_1 + k_2$, $\Delta k = k_0 - k'$, and $H = \frac{1 + \epsilon'^2}{k'' - ik'\epsilon'} - i\frac{\epsilon' - \epsilon}{k'}$, k_0, k_1, and k_2 are the wave vectors of the ω_0, ω_1, and ω_2 fields, respectively.

Fig. 4(c) shows the IR intensities simulated with two pump wavelengths, 0.8 and 1.9 μm, as a function of the angle from the propagation axis. We have calculated the field at $z = 380$ mm with the parameters $b = 38$ mm and $f = 190$ mm for both the pump wavelengths. The better beam quality is due to the smaller phase mismatch for longer pump wavelength. At the same time, we can expect better conversion efficiency. It would be possible to generate much higher intensity IR pulses by using the FWDFG with longer wavelength pump pulses.

D. CEP Stability

In theory, the CEP of the generated IR pulse is passively stabilized in the present scheme. Following the expression of the CEP in frequency conversion processes described in [9] and [51], the phase of the generated IR pulse produced through the process, $\omega_1 + \omega_1 - \omega_2 \rightarrow \omega_0$, is given by $\phi_0 = \pi/2 + \phi_1 + \phi_1 - \phi_2$, where ϕ_0, ϕ_1, and ϕ_2 are the phases of ω_0, ω_1, and ω_2 components, respectively. Since ω_2 wave was produced through SH of ω_1 wave, the phase of the ω_2 wave is given by $\phi_2 = \pi/2 + 2\phi_1$. Therefore, ϕ_0 must be 0, which fact means that the CEP of the IR pulse is automatically stabilized even without CEP stabilization of the input pulse. However, it is important to check the CEP stability experimentally since the fluctuation of the delay between the fundamental and SH pulses and/or some noise of the input pulse can affect the CEP stability [39], [52], [53].

The CEP stability measurement of the IR pulses ($E_{\text{IR}}(t)$) can be realized by measuring the interference between the SH of a reference pulse ($E_{\text{shg}}(t) \propto E_{\text{ref}}^2(t)$) and the FWDFG
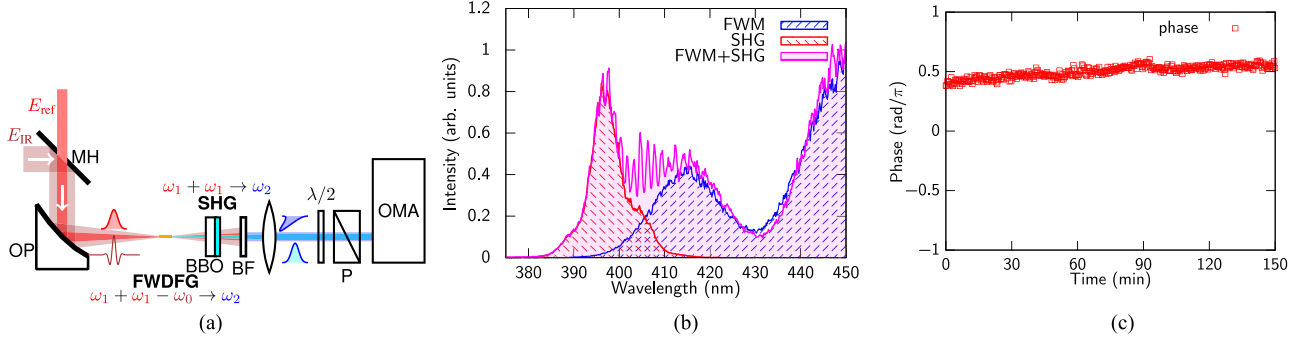
Fig. 5. (a) Schematic of the experiment for the measurement of the CEP stability. MH: alminium-coated mirror with a hole ($\phi = 7$ mm), OP: aluminium-coated off-axis parabolic mirror ($f = 150$ mm), BBO: β-barium borate crystal ($\theta = 29°$, $t = 50$ μm) on a 2-mm thick fused silica substrate, $\lambda/2$: half wave plate, BF: blue filter (FGB37, Thorlabs), P: calcite polarizer, OMA: spectrometer for ultraviolet region (USB2000+, Ocean Optics). (b) Interference signal between the SH of the reference pulse and the FWM signal. (c) Time evolution of the phase of the interference fringe.

signal ($E_{\text{fwm}}(t) \propto E_{\text{ref}}^2(t)E_{\text{IR}}^*(t)$) of the reference and IR pulses. The interference signal is explained as a cross-term of $|E_{\text{shg}}(t) + E_{\text{fwm}}(t)|^2$, namely, $E_{\text{shg}}^*(t)E_{\text{fwm}}(t)$. The phase of the interference signal is written as $-\phi_{\text{shg}} + \phi_{\text{fwm}} = -(\pi/2 + 2\phi_{\text{ref}}) + (\pi/2 + 2\phi_{\text{ref}} - \phi_{\text{IR}}) = -\phi_{\text{IR}}$, where ϕ_{x} denotes the CEP of E_{x} for each subscript. From the equation, it is clear that the phase drift of the interference signal reflects that of the CEP of the IR pulse. This scheme is essentially the same as that described in [54].

The experimental setup is shown in Fig. 5(a). The reference pulse is a small portion of the output from the Ti:sapphire amplifier. The pulse duration and the center wavelength of the reference pulse are 30 fs and 800 nm, respectively. A β-barium borate crystal (BBO, $\theta = 29°$, $t = 50$ μm) on a 2-mm thick fused silica substrate was inserted behind the focus where the FWDFG signal was generated as is shown in Fig. 5(a). The crystal was placed in a way that the pulses enter from the back side, i.e., from the substrate side. This way, the FWDFG signal is delayed by ~300 fs relative to the reference pulse due to the group delay difference in the substrate before entering the BBO crystal. A half-wave plate and a calcite polarizer were inserted behind the crystal to optimize the intensity ratio between the SH and FWM signals. In Fig. 5(b) the observed interference fringe is shown. The fringe spacing was about 3 THz, which corresponds to the expected delay between the reference pulse and the FWM signal. The phase of the fringe was reasonably stable for hours without any feedback loop. The results of the phase measurements are shown in Fig. 5(c). The shot-to-shot instability of the phase was estimated as 78 mrad rms over 100 shots (in 0.1 s) and 154 mrad rms for 2.5 h.

III. WAVEFORM CHARACTERIZATION

In order to quantitatively evaluate the temporal shape of the phase-stable IR pulse, we did FROG-CEP measurement. The detail of the concept of FROG-CEP is shown in [27]. Briefly summarizing, simultaneous measurement of FROG [55], [56] and EOS [57] gives us full information of the waveform of the ultrashort pulse. More concretely, we obtain the amplitude and the relative spectral phase from the FROG signal and the CEP value from the EOS signal. The complete waveform of the

ultrashort pulse can be retrieved by using these values. Considering the frequency range of our IR pulse, a combination between the cross-correlation FWDFG FROG [17], [24], [58] and air-biased coherent detection [59] is one of the best way to realize the FROG-CEP measurement.

A. Experimental Setup

The experimental setup is shown in Fig. 6(a). The IR pulse was combined with a small portion of the fundamental pulse ($E_{\text{ref}}(t - \tau)$, 15 μJ, 30 fs) with a delay time τ through a mirror with a hole. The combined beam was focused into nitrogen with an aluminium-coated parabolic mirror ($f = 150$ mm). The polarizations of the reference and IR pulses were perpendicular to each other, and the polarization of the generated FWDFG signal, $E_{\text{fwm}}(t, \tau) \propto E_{\text{ref}}^2(t - \tau)E_{\text{test}}^*(t)$, was parallel to the sub-single-cycle pulse and perpendicular to the reference pulse. To produce second harmonic (SH, $E_{\text{ref}}^2(t)$) of the reference pulse, a bias field was applied to Rogowski-type electrodes[60] with a distance of 3 mm by two high voltage amplifiers (HEOPS-5B6, Matsusada) with an amplitude of ± 4 kV and a frequency of 500 Hz, which is synchronized with the 1 kHz repetition rate of the laser pulse train. The direction of the electric field was parallel to the reference pulse, and the FWDFG signal and the bias induced SH have polarizations perpendicular to each other.

The intensity of the mixed fields of FWDFG and SH is essentially obtained as follows:

$$\left\langle \left| E_{\text{ref}}^2(t - \tau) + \alpha E_{\text{ref}}^2(t - \tau)E_{\text{test}}^*(t) \right|^2 \right\rangle$$
$$= \left\langle \left| E_{\text{ref}}^2(t - \tau) \right|^2 \right\rangle + \left\langle |\alpha|^2 \left| E_{\text{ref}}^2(t - \tau)E_{\text{test}}^*(t) \right|^2 \right\rangle$$
$$+ \left\langle 2\Re \left\{ \alpha E_{\text{ref}}^{*2}(t - \tau)E_{\text{ref}}^2(t - \tau)E_{\text{test}}^*(t) \right\} \right\rangle, \quad (2)$$

where $\langle \rangle$ denotes time average and α is a constant proportional to the nonlinear susceptibility of the FWDFG, which is assumed as an instantaneous process. τ is the delay between the reference and test pulses. The first term is independent of the delay time. The second term is the intensity cross-correlation signal between the test and reference pulses. If the second term is spectrally resolved, it yields an FWDFG XFROG signal [17], [24], [58]. The third term is the EOS signal, in other words, the interference
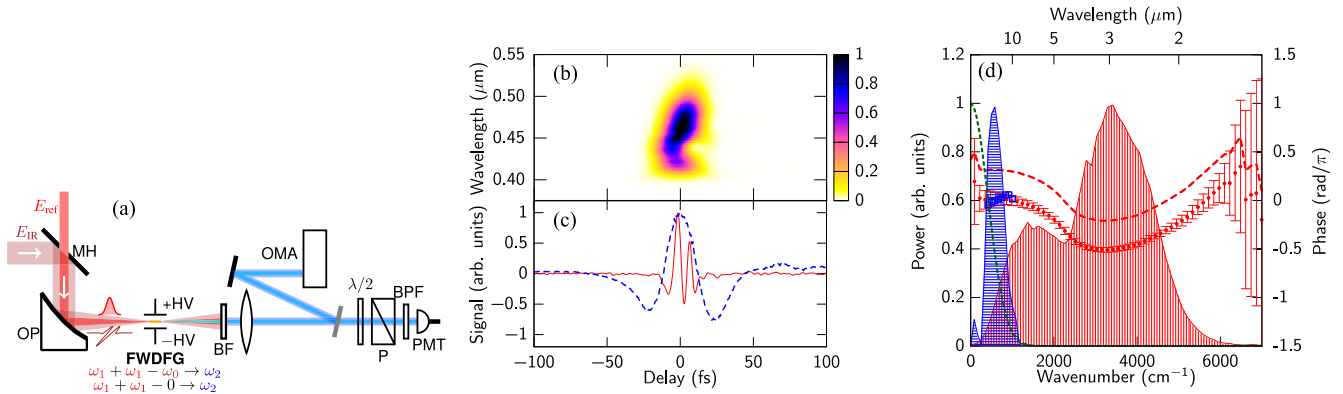
Fig. 6.   (a) Schematic of the experiment for the waveform measurement, FROG-CEP. MH: alminium-coated mirror with a hole ($\phi = 7$ mm), OP: aluminium-coated off-axis parabolic mirror ($f = 150$ mm), BF: blue filter (FGB37, Thorlabs), $\lambda/2$: half wave plate, P: calcite polarizer, BPF: bandpass filter at 400 nm (10 nm FWHM), OMA: spectrometer for ultraviolet region (USB2000+, Ocean Optics). (b) The XFROG trace and (c) EOS signal (dashed curve) measured in the experiment. The solid curve shows the electric field reconstructed with the method described in the text. (d) The shaded (vertically hatched) and dashed curves are the spectral distribution and phase profile obtained with XFROG. The dots are the spectral phase after the offset correction. The offset of the spectral phase is corrected by using the phase information obtained with EOS. The error bars of the phase are estimated with the bootstrap method described in the text. The shaded (horizontally hatched) curve and open squares are the spectral distribution and spectral phase obtained from the Fourier transform of the EOS signal (dashed curve in (b)). The densely dashed curve shows the filtering function for the EOS signal, which is Fourier transform of $\left| E_{\mathrm{ref}}^2(t) \right|^2$. The FROG error was 0.3% on a 512×512 grid.

between a local oscillator field ($E_{\mathrm{ref}}(t - \tau)$) and a nonlinear field ($E_{\mathrm{ref}}(t - \tau)E_{\mathrm{test}}^2(t)$).

We measured the second and third terms separately by using the following method. The beam generated through the nonlinear interactions was split by a beam splitter (sapphire plate) with nearly normal incidence. The reflected beam (∼7%) was detected with a conventional spectrometer for XFROG, namely, recording the second term of eq. (2). The transmitted beam was used for recording the EOS signal, namely the third term of eq. (2). The transmitted orthogonally polarized SH and FWDFG signals were mixed with a zero-order half wave plate (WPH10M-405, Thorlabs) and the horizontally polarized component was selected through a calcite polarizer. After passing through a bandpass filter at 400 nm (10 nm FWHM), the beam was detected with a photomultiplier tube (H10721-210, Hamamatsu). Interference between the SH and FWDFG signal was detected through a lock-in amplifier (SR830, Stanford Research) referenced with the modulation frequency of the high voltage (500 Hz). The interference signal does not affect the XFROG signal since the interference signal is much smaller than the FWDFG signal (<10% at 400 nm) and the integration time of the spectrometer (0.1 s) is much longer than the period of the modulation frequency of the high voltage. The required reference pulse energy for a reasonable signal-to-noise ratio was ∼2 μJ with the current condition, too.

B. Waveform Retrieval

One example of the data set is shown in Fig. 6(b)–(d). Fig. 6(b) shows measured traces of spectra corresponding to the second term in eq. (2), and the dashed curve in Fig. 6(c) shows the measured signal corresponding to the third term in eq. (2). The process of the field retrieval is as follows. (i) The intensity and (relative) phase of the test pulse in frequency-domain (the vertically hatched and dashed curves in Fig. 6(d)) are obtained from

Fig. 6(b) through an XFROG retrieval algorithm. The offset of the phase cannot be determined at this stage. (ii) The intensity and phase of the electric field in frequency-domain (the horizontally hatched curve and open squares in Fig. 6(d)) are obtained through Fourier transform of the EOS signal (the dashed curve in Fig. 6(c)). (iii) The spectral phase obtained with the XFROG is corrected by shifting it so that the spectral phases from XFROG and EOS match in the overlapped region, from 300 cm^{-1} to 1000 cm^{-1}, as the closed circles in Fig. 6(d). (iv) The electric field of the generated IR pulse is obtained with the corrected phase value as the solid curve in Fig. 6(c). The full width at half maximum of the intensity in time-domain was 6.9 fs at 3000 cm^{-1} center frequency. Since the period of the center frequency is 11 fs, the cycle number of the pulse is 0.63, which means that the IR pulse is a sub-single-cycle pulse, or even close to a half-cycle pulse. The absolute phase at 3000 cm^{-1} was obtained as -0.51π.

C. Nonlinear Chirp of the Single-Cycle Pulse

It can be seen that the spectral phase changes rapidly around 2200 cm^{-1}. We believe that the nonlinear chirp is due to interference between two parametric processes. In the following paragraph, we explain the detail of the interference.

The third-order nonlinear polarization is proportional to the cube of the input fields, $(E_1(t) + E_2(t))^3$, assuming perfect phase matching. When the fundamental and SH electric fields are $E_1(t) = \mathcal{E}_1(t) \exp(i\omega_1 t + i\phi_1) + \text{c.c.}$ and $E_2(t) = \mathcal{E}_2(t) \exp(i\omega_2 t + i\phi_2) + \text{c.c.}$, respectively, the low frequency components of the nonlinear polarization, $p_{\mathrm{NL}}(t)$, can be written as

$$p_{\mathrm{NL}}(t) \propto \mathcal{E}_1^2(t)\mathcal{E}_2^*(t) \exp\big(i(2\omega_1 - \omega_2)t\big) + \text{c.c.}$$
$$= \mathcal{P}_{\mathrm{NL}}(t) \exp(i\omega_0 t) + \text{c.c.} \qquad (3)$$
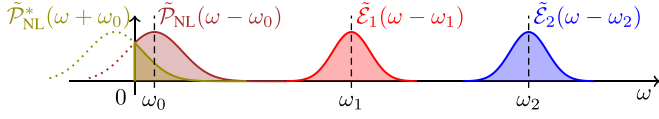
Fig. 7. Spectral overlap of the nonlinear polarizations from two parametric processes, $\omega_1 + \omega_1 - \omega_2 \rightarrow \omega_0$ and $\omega_2 - \omega_1 - \omega_1 \rightarrow \omega_0$. $\tilde{\mathcal{E}}_1(\omega)$ and $\tilde{\mathcal{E}}_2(\omega)$ are Fourier transform of $\mathcal{E}_1(t)$ and $\mathcal{E}_2(t)$, respectively.

where $\mathcal{P}_{\mathrm{NL}}(t) = \mathcal{E}_1^2(t)\mathcal{E}_2^*(t)$, $\omega_0 = 2\omega_1 - \omega_2$. The electric fields are not complex but real from this subsection to explain the situation clearly. The Fourier transform of eq. (3) can be written as

$$\tilde{p}_{\mathrm{NL}}(\omega) \propto \tilde{\mathcal{P}}_{\mathrm{NL}}(\omega - \omega_0) + \tilde{\mathcal{P}}_{\mathrm{NL}}^*(\omega + \omega_0), \qquad (4)$$

where $\tilde{p}_{\mathrm{NL}}(\omega)$ and $\tilde{\mathcal{P}}_{\mathrm{NL}}(\omega)$ mean Fourier transform of $p_{\mathrm{NL}}(t)$ and $\mathcal{P}_{\mathrm{NL}}(t)$, respectively. We can say that $\tilde{\mathcal{P}}_{\mathrm{NL}}(\omega - \omega_0)$ and $\tilde{\mathcal{P}}_{\mathrm{NL}}^*(\omega + \omega_0)$ come from $\omega_1 + \omega_1 - \omega_2 \rightarrow \omega_0$ and $\omega_2 - \omega_1 - \omega_1 \rightarrow \omega_0$ processes, respectively. Normally, when $\tilde{\mathcal{P}}_{\mathrm{NL}}(\omega - \omega_0)$ has some finite value in a positive frequency region, $\tilde{\mathcal{P}}_{\mathrm{NL}}^*(\omega + \omega_0)$ has some finite value only in a negative frequency region, and vice versa. However, when the bandwidth of $\tilde{\mathcal{P}}_{\mathrm{NL}}(\omega)$ is comparable to ω_0, $\tilde{\mathcal{P}}_{\mathrm{NL}}(\omega - \omega_0)$ and $\tilde{\mathcal{P}}_{\mathrm{NL}}(\omega + \omega_0)$ have some overlap in a positive frequency region and it can interfere with each other as is shown in Fig. 7.

The nonlinear chirp at around 2200 cm^{-1} could not be compensated with any delay between the fundamental and SH. The reason is that the residual chirp of the light source is significant to be compensated in the whole frequency range. We can also observe that the direction of the chirp is opposite in high and low frequency components, which is consistent with the fact that the two parametric processes must have the opposite chirp. The interference effect eventually becomes important for CEP control of the sub-single-cycle pulse. We come back to the point in the next section.

D. Accuracy of the Waveform Measurement

The accuracy of the spectral phases in the overlapped region obtained from the FROG and the EOS signals directly affects the accuracy of the waveform characterization. The phase obtained from the EOS signal can be very precisely defined since the oscillation period of the signal is much longer than the precision of the delay stage. The statistical error of the phase value from the EOS signal estimated through several measurements was ∼0.01π. Determining the error of the spectral phase obtained from FROG is not so straightforward since the relationship between the measured data and retrieved values is complex in FROG. Here we have obtained the error bars by using a bootstrap method [61], which is a well-established statistical resampling tool for determining uncertainty and has already been applied for estimation of error bars of phases obtained from FROG [62], [63]. We have estimated the standard deviation of the phase in the overlapped region as 0.06π (see Fig. 6(d)), therefore, the accuracy of the CEP is estimated as ±0.07π.

Note that the slopes of the phases in the overlapped region coincide within the error bars, which means that the group delays

from the two independent measurements are matched with each other. This fact strongly supports the consistency of the data sets.

IV. CEP CONTROL

In passive stabilization schemes, the CEP is controlled by manipulating the relative phase between the two input pulses for the difference frequency generation [54], [64]. Very recently, it has been shown that the phase of the IR pulse generated through two-color filamentation behaves differently although the CEP of the IR pulse is also passively stabilized [65]. In this section, we show the detailed investigation of CEP control of IR pulses generated through two-color filamentation.

A. Preliminary Theory

Here we use a 1-D model with perfect phase matching. Assuming that the two input electric fields are $E_1(t) = \mathcal{E}_1(t)\exp(i\omega_1 t + i\phi_1) + \text{c.c.}$ and $E_2(t) = \mathcal{E}_2(t)\exp(i\omega_2 t + i\phi_2) + \text{c.c.}$, the third-order nonlinear polarization for the IR pulse generation process, $p_{\mathrm{NL}}(t)$, can be written as

$$p_{\mathrm{NL}}(t) \propto \mathcal{E}_1^2(t)\mathcal{E}_2^*(t)\exp\big(i(2\omega_1 - \omega_2)t + i(2\phi_1 - \phi_2)\big) + \text{c.c.}$$
$$= \mathcal{P}_{\mathrm{NL}}(t)\exp(i\omega_0 t + i\Delta\phi) + \text{c.c.} \qquad (5)$$

where $\mathcal{P}_{\mathrm{NL}}(t) = \mathcal{E}_1^2(t)\mathcal{E}_2^*(t)$, $\omega_0 = 2\omega_1 - \omega_2$, and $\Delta\phi = 2\phi_1 - \phi_2$. Assuming that $\ddot{p}_{\mathrm{NL}}(t)$ is the far-field point source, the generated field, $E_0(t)$, can be written as

$$E_0(t) \propto \ddot{p}_{\mathrm{NL}}(t)$$
$$= \big(\ddot{\mathcal{P}}_{\mathrm{NL}}(t) + i2\omega_0\dot{\mathcal{P}}_{\mathrm{NL}}(t) - \omega_0^2\mathcal{P}_{\mathrm{NL}}(t)\big)$$
$$\cdot \exp(i\omega_0 t + i\Delta\phi) + \text{c.c.} \qquad (6)$$

When the variation of the envelope of the FWDFG signal is slower than the oscillation of the generated polarization, namely, $\ddot{\mathcal{P}}_{\mathrm{NL}}(t) \ll \omega_0\dot{\mathcal{P}}_{\mathrm{NL}}(t) \ll \omega_0^2\mathcal{P}_{\mathrm{NL}}(t)$, the output field of the FWDFG can be written as $\omega_0^2\mathcal{P}_{\mathrm{NL}}(t)\cos(\omega_0 t + \Delta\phi)$. In this case, the CEP of the field is $\Delta\phi$, which means that the relative phase between the two input pulses directly affects the CEP of the output pulse. This situation is basically the same at three-wave DFG.

On the other hand, when the variation of the envelope of the FWDFG signal is faster than the oscillation of the generated polarization ($\omega_0 \sim 0$), namely, $\ddot{\mathcal{P}}_{\mathrm{NL}}(t) \gg \omega_0\dot{\mathcal{P}}_{\mathrm{NL}}(t) \gg \omega_0^2\mathcal{P}_{\mathrm{NL}}(t)$, the field of the FWDFG reduces to $\ddot{\mathcal{P}}_{\mathrm{NL}}(t)\exp(i\Delta\phi) + \text{c.c.}$ In this case, the oscillation of the generated field comes from the time derivative of $\mathcal{P}_{\mathrm{NL}}(t)$. As a result, $\Delta\phi$ does not contribute to the phase but to the amplitude of the output field. This is basically the same as four-wave optical rectification process described in [11], [38], and [39].

The above discussion suggests that the phase behavior depends on the generated frequency. The transition between the two of the phase behavior can be considered as the transition between FWDFG and four-wave optical rectification. Such transition had never been discussed before [66] even in theory. The reason would be that the transition could be visible only for
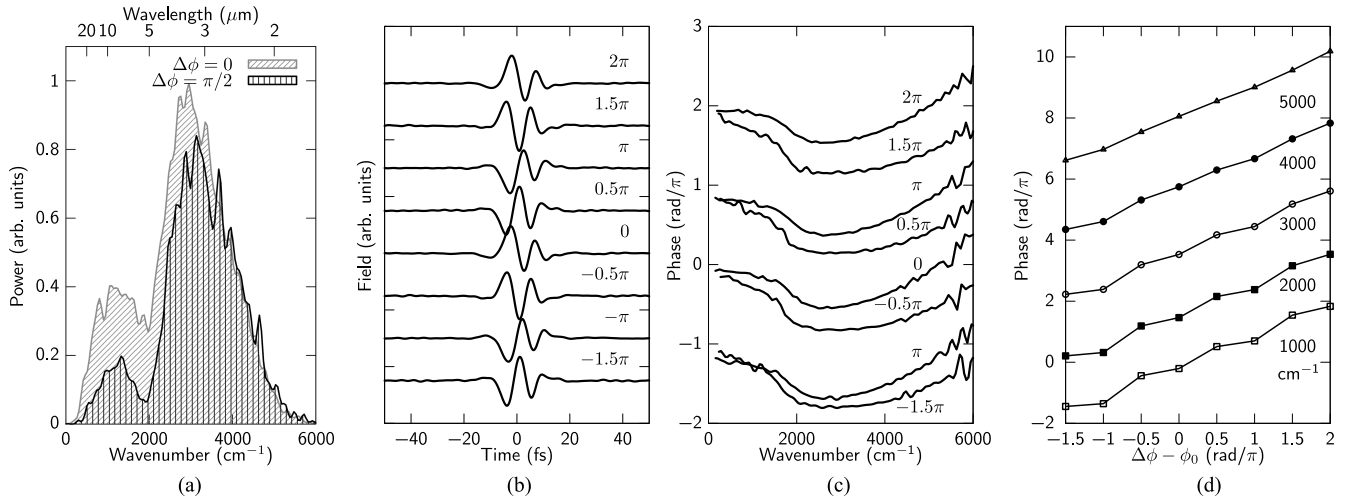
Fig. 8. (a) The power spectra of the generated IR pulses for two different relative phase of the input pulses. (b) Waveforms and (c) spectral phases of the generated IR pulses at each relative phase, respectively. (d) The relative phase dependence of the phases of the IR pulses for each frequency component. There are 2π offsets between the curves.

supercontinuum spreading over several octaves which has become available very recently.

Such transition can be defined also for three-wave mixing processes, namely $\chi^{(2)}$ processes. Assuming that the same input fields in eq. (5), the nonlinear polarization for three-wave difference frequency generation process, $p_{\mathrm{NL}}(t)$, can be written as

$$p_{\mathrm{NL}}(t) \propto \mathcal{E}_1(t)\mathcal{E}_2^*(t) \exp\big(i(\omega_1 - \omega_2)t + i(\phi_1 - \phi_2)\big) + \text{c.c.}$$
$$= \mathcal{P}_{\mathrm{NL}}(t) \exp(i\omega_0 t + i\Delta\phi) + \text{c.c.} \qquad (7)$$

where $\mathcal{P}_{\mathrm{NL}}(t) = \mathcal{E}_1(t)\mathcal{E}_2^*(t)$, $\omega_0 = \omega_1 - \omega_2$, and $\Delta\phi = \phi_1 - \phi_2$. From this equation, it is easy to understand that the same amplitude and phase behavior as the $\chi^{(3)}$ process can be seen. However, such amplitude and phase behavior for the $\chi^{(2)}$ process ends up to be just linear interference effect between $E_1(t)$ and $E_2(t)$. When the spectra of $E_1(t)$ and $E_2(t)$ are completely separated with each other, there is no interference between the two fields and $\Delta\phi$ contributes to only the phase of $p_{\mathrm{NL}}(t)$ in eq. (7). On the other hand, when the spectra of $E_1(t)$ and $E_2(t)$ are well overlapped with each other, ω_0 becomes naturally zero and $\Delta\phi$ defines whether the interference between the two fields is constructive or destructive. As a result, $\Delta\phi$ contributes to the amplitude of $p_{\mathrm{NL}}(t)$. Therefore, it is not very valuable to discuss the phenomenon at the three-wave mixing processes.

In contrast, the amplitude and phase behavior at the four-wave mixing processes is related to f-to-$2f$ interferometer, which is important for ultrafast science. Such interference effect has already been used for the CEP detection with THz generation in gases [67], [68].

B. Experimental Details

We measured the waveforms of the sub-single-cycle pulses at several different delay plate angles by using FROG-CEP. Before discussing the results of the waveforms, we would like to explain the relative phase dependence of the power spectrum of the sub-single-cycle pulse. We observed that the intensity of the sub-single-cycle pulse changed periodically with the angle of the delay plate. Fig. 8(a) shows the power spectra of the sub-single-cycle pulses at two different angles of the delay plate. We have defined that the relative phase $\Delta\phi$ is 0 and $\pi/2$ when the intensity is maximum and minimum, respectively. The absolute value of $\Delta\phi$ cannot be determined in this experiment. However, the relative difference can be obtained by the difference of the angle of the crystal. The $\Delta\phi$ dependence of the intensity is stronger for low frequency components ($<2500\ \mathrm{cm}^{-1}$) whereas the high frequency components ($>2500\ \mathrm{cm}^{-1}$) are much less sensitive to $\Delta\phi$.

Fig. 8(b) and (c) shows waveforms and spectral phases of the sub-single-cycle pulses at different relative phases of the input pulses, respectively. The absolute value of the spectral phase has significance in this experiment since we measured complete waveform of the sub-single-cycle pulse. Fig. 8(d) shows phase change of the sub-single-cycle pulses at several different frequencies. The phase of the high frequency components ($\omega_0 > 3000\ \mathrm{cm}^{-1}$) changes continuously and linearly with respect to $\Delta\phi$. On the other hand, the phase of the low frequency components ($\omega_0 < 3000\ \mathrm{cm}^{-1}$) changes by π like a step function, which means that $\Delta\phi$ basically affects only the amplitude. The π phase jump means that only the sign of the amplitude (the sign of $\cos\Delta\phi$) changes.

C. Numerical Simulations

It is interesting to reproduce the transition between the two scenarios by numerical simulations. There are two basic physical models to explain the IR generation through two-color laser filamentation. One is based on FWDFG of the two-color input pulses [11], [13], [39] and the other is a photocurrent model that accounts for electron motion in the two-color input field [41], [68].

1) Four-Wave Difference Frequency Generation Model: At first, we describe the FWDFG model. We have simply calculated $\big(\mathcal{E}_1(t)\exp(i\omega_1 t)+\mathcal{E}_2(t)\exp(i\omega_2 t - i\Delta\phi) + \text{c.c.}\big)^3$, taken second derivative, and picked up only the low frequency
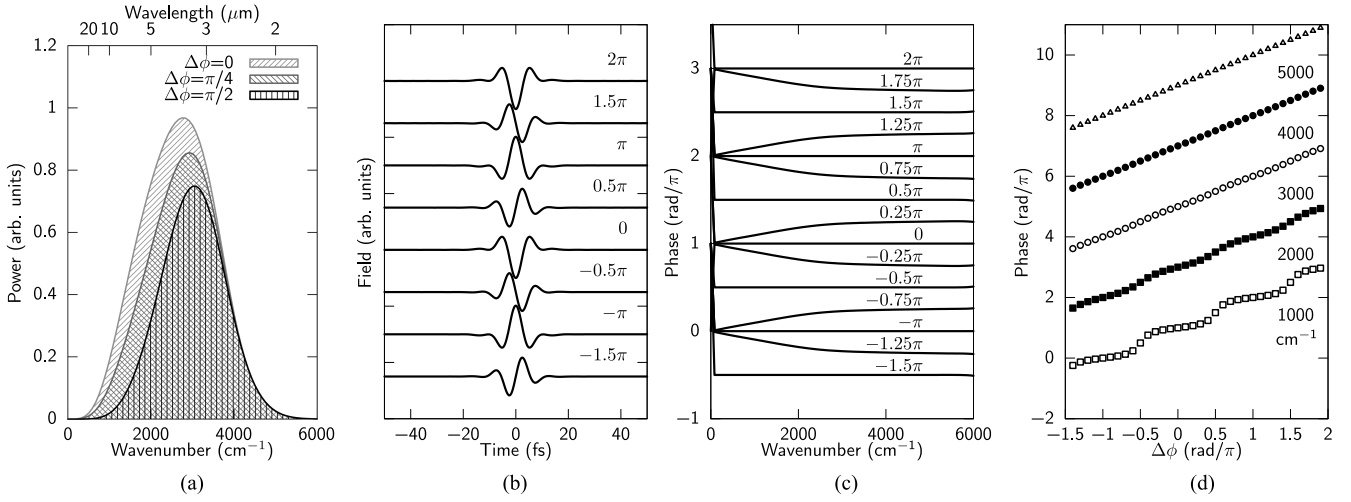
Fig. 9. Results of the numerical simulations based on the FWDFG model. (a) The power spectra, (b) waveforms and (c) spectral phases of the generated IR pulses at each relative phase, respectively. (d) The relative phase dependence of the phases of the IR pulses for each frequency component. There are 2π offsets between the curves.

component. The input electric fields were calculated from the inverse fourier-transform of the spectra of the two-color pulses after the filamentation. We assumed no chirp for both the pulses in the simulation. Fig. 9 shows the results of the numerical simulations. The stepwise variation of the phase and the phase dependence of the power spectrum is clearly reproduced with the simulations (see Fig. 9(a) and (d)). Interestingly, some "artificial" chirp appear in the low frequency region (<2000 cm⁻¹ in Fig. 9(c)) where $\Delta\phi$ is between half-integer multiple of π and integer multiple of π. It is clear that this chirp is caused by the frequency dependence of the CEP variation.

2) Photocurrent Model: Next we consider a photocurrent model to explain the CEP behavior at the sub-single-cycle pulse generation through two-color filamentation. Such interpretation has been suggested in [41] for the first time and the model is widely used to explain such THz generation.

We performed numerical simulations as follows. Here we employ static tunneling ionization [68], and the ionization rate $W(t)$ can be written as

$$W(t) = \frac{\alpha}{\hat{E}(t)} \exp\left(-\frac{\beta}{\hat{E}(t)}\right), \qquad (8)$$

where $\hat{E}(t) = |E(t)|/E_a$ is the optical field strength in atomic units, $E_a \sim 5.14 \times 10^{11}$ V/m, $\alpha = 4\omega_a r_H^{5/2}$, $\beta = (2/3)r_H^{3/2}$, $\omega_a = 4.13 \times 10^{16}$ s⁻¹ is atomic frequency unit, $r_H = U_{ion}^{N_2}/U_{ion}^{H} \sim 15.6/13.6$ eV is the ionization potential of nitrogen molecules at standard pressure under consideration relative to that of hydrogen. Given the nominal ionization rate $W(t)$, the generated plasma density $\rho(t)$ is then the solution of the rate equation,

$$\dot{\rho}(t) = W(t)\left(\rho_0 - \rho(t)\right). \qquad (9)$$

Hence the far-field emission source $\ddot{p}(t)$ can be written as [19]

$$\ddot{p}(t) = \frac{e^2}{m}e^{-t/\tau_s}\left[I_\rho(t)E(t) - \frac{1}{\tau_s}\int_{-\infty}^{t}dt' I_\rho(t')E(t')\right] \quad (10)$$

where $I_\rho(t) = \int_{-\infty}^{t}dt'\dot{\rho}(t')\exp\left(t'/\tau_s\right)$. τ_s is the scattering time of the electrons, which is assumed to be 190 fs [69]. We substitute the input field as $E(t) = \mathcal{E}_1(t)\exp\left(i\omega_1 t\right) + \mathcal{E}_2(t)\exp\left(i\omega_2 t - i\Delta\phi\right) + $ c.c. The input field is the same as the simulation with the FWDFG model, namely, the inverse fourier-transform of the spectra of the two input pulses after the filamentation. The amplitude of the field was set to 4.18×10^{10} V/m, which is estimated from the experimental condition. The plasma density calculated with the strength of the field is $0.24\,\rho_0$ (where $\rho_0 = 2.7 \times 10^{19}$ cm⁻³ is the molecular density).

Fig. 10 shows the results of the numerical simulations. The stepwise variation of the phase and the phase dependence of the power spectrum are reproduced from the simulations (see Fig. 10(a) and (d)) in a similar way as the FWM model. The relationship between the envelope and the generated frequency causes the frequency dependence of the phase variation. Although the power of the sub-single-cycle pulse is very sensitive to the input pulse intensity, it has no influence to the phase variation. Preliminary simulation of such power and phase behavior of the THz waveform was previously reported in [70].

D. Discussion

There is a significant difference in the absolute value of $\Delta\phi$ between the two models. In the FWDFG model, the amplitude is maximum at $\Delta\phi = n\pi$ and the CEP transition occurs at $\Delta\phi = (n + 1/2)\pi$. In contrast, the amplitude is maximum at $\Delta\phi = (n + 1/2)\pi$ and the CEP transition occurs at $\Delta\phi = n\pi$ in the photocurrent model. Such contrast between the two models is consistent with previous reports [41], [68].

If the contributions from two models were about equal, such power and CEP behavior would disappear. However, the behavior has been clearly observed in the experiment. This means that one of the two models are at least dominant for the generation process. It would be possible to determine the model if we can measure the absolute value of $\Delta\phi$. However, measurement of $\Delta\phi$ at the generation point is a very difficult
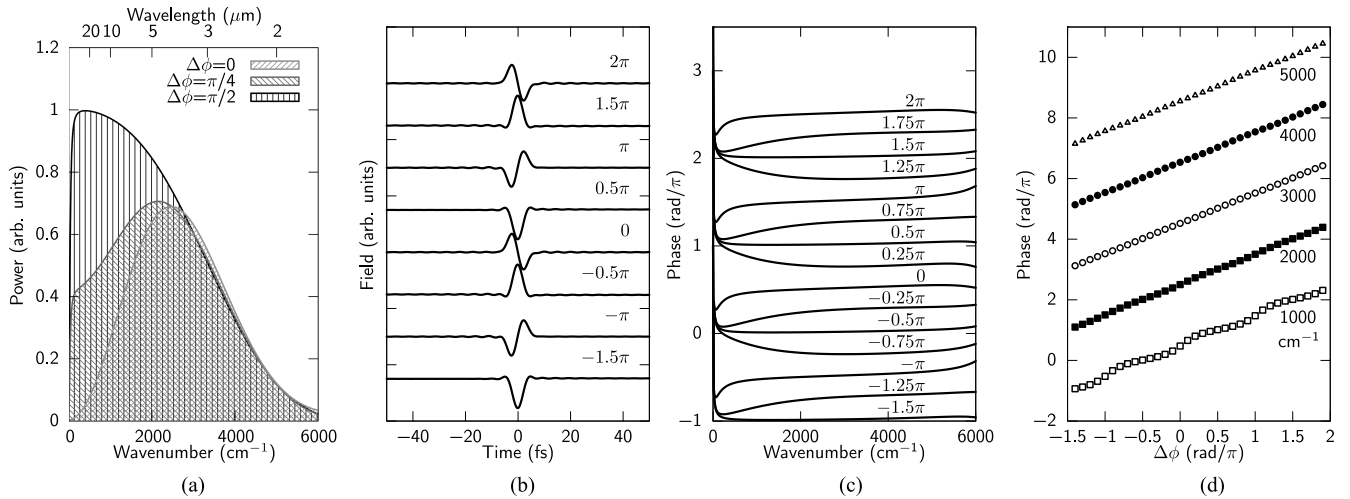
Fig. 10. Results of the numerical simulations based on the photocurrent model. (a) The power spectra, (b) waveforms and (c) spectral phases of the generated IR pulses at each relative phase, respectively. (d) The relative phase dependence of the phases of the IR pulses for each frequency component. There are 2π offsets between the curves.

task. In [71] the authors have claimed that $\Delta\phi$ at the generation point was successfully obtained and concluded that the photocurrent model is the dominant process for the THz generation through two-color filamentation. However, $\pi/2$ phase shift at SHG [72] and Gouy phase shift are not taken into account at the phase determination. We believe that more careful investigation is necessary to determine which model is dominant for the IR pulse generation through two-color filamentation.

V. CONCLUSION

In conclusion, ultrabroadband coherent IR spectrum which covered the entire IR region was generated through two-color filamentation. The spectrum spread from 400 to 5500 cm^{-1}, which corresponds to more than 3.5 octave with full width at tenth maximum. The waveform of the IR pulse was measured by using FROG-CEP. The duration of the IR pulse was 6.9 fs, which corresponds to nearly half cycles of 3000 cm^{-1} carrier frequency. The instability of the CEP was estimated as 154 mrad rms in 2.5 h.

The CEP of the sub-single-cycle pulses generated through two-color filamentation has been investigated in detail by using FROG-CEP. It has been found that the relative phase dependence of the CEP is different depending on the generated frequency. The phase of the high frequency components is proportional to the relative phase between the two-color pulses, which is the same as DFG or idler of optical parametric amplifier. However, the phase of the low frequency components changes as a step function. The phase behavior can be explained by both FWDFG and photocurrent models. The transition of the phase behavior has been clearly observed.

We believe that these findings are useful for development of phase-stable sub-single-cycle pulse generation. For example, the CEP at optical rectification would be even more robust than that at DFG since it does not depend on the delay between the two input pulses. Some artificial chirp might appear under some particular phase relationship between the two input pulses.

In the current condition, the energy of the sub-single-cycle pulse was ~0.5 μJ. With this energy level, it is not possible to apply the pulses for high harmonic generation but possible for linear or nonlinear spectroscopy for condensed matters. Actually, we have applied the light source for high speed IR absorption spectroscopy [21], [36] and for ultrafast pump-probe spectroscopy [23].

According to our numerical simulation, longer wavelength input pulses would dramatically improve the beam quality and efficiency. It would become possible to generate intense sub-single-cycle pulses through two-color filamentation with longer wavelength input pulses (~2 μm) and to use them for high harmonic generation in the future.

REFERENCES

[1] M. Y. Shverdin, D. R. Walker, D. D. Yavuz, G. Y. Yin, and S. E. Harris, "Generation of a single-cycle optical pulse," *Phys. Rev. Lett.*, vol. 94, p. 033904, 2005.

[2] H.-S. Chan *et al.*, "Synthesis and measurement of ultrafast waveforms from five discrete optical harmonics," *Science*, vol. 331, pp. 1165–1168, 2011.

[3] H.-S. Chan, Z.-M. Hsieh, L.-H. Peng, and A. H. Kung, "Compact optical function generator," *Opt. Lett.*, vol. 37, pp. 2805–2807, 2012.

[4] G. Krauss *et al.*, "Synthesis of a single cycle of light with compact erbium-doped fibre technology," *Nature Photon.*, vol. 4, pp. 33–36, 2010.

[5] S.-W. Huang *et al.*, "High-energy pulse synthesis with sub-cycle waveform control for strong-field physics," *Nature Photon.*, vol. 5, pp. 475–479, 2011.

[6] S.-W. Huang *et al.*, "Optical waveform synthesizer and its application to high-harmonic generation," *J. Phys. B, Atomic, Mol. Opt. Phys.*, vol. 45, pp. 074009-1–074009-14, 2012.

[7] A. Wirth *et al.*, "Synthesized light transients," *Science*, vol. 334, pp. 195–200, 2011.

[8] M. T. Hassan *et al.*, "Invited article: Attosecond photonics: Synthesis and control of light transients," *Rev. Sci. Instrum.*, vol. 83, pp. 111301-1–111301-19, 2012.

[9] A. Baltuška, T. Fuji, and T. Kobayashi, "Controlling the carrier-envelope phase of ultrashort light pulses with optical parametric amplifiers," *Phys. Rev. Lett.*, vol. 88, p. 133901, 2002.

[10] T. Fuji, A. Apolonski, and F. Krausz, "Self-stabilization of carrier-envelope offset phase by use of difference-frequency generation," *Opt. Lett.*, vol. 29, pp. 632–634, 2004.

[11] D. J. Cook and R. M. Hochstrasser, "Intense terahertz pulses by four-wave rectification in air," *Opt. Lett.*, vol. 25, pp. 1210–1212, 2000.

[12] M. Clerici *et al.*, "Wavelength scaling of terahertz generation by gas ionization," *Phys. Rev. Lett.*, vol. 110, p. 253901, 2013.

[13] T. Bartel, P. Gaal, K. Reimann, M. Woerner, and T. Elsaesser, "Generation of single-cycle THz transients with high electric-field amplitudes," *Opt. Lett.*, vol. 30, pp. 2805–2807, 2005.

[14] T. Fuji and T. Suzuki, "Generation of sub-two-cycle mid-infrared pulses by four-wave mixing through filamentation in air," *Opt. Lett.*, vol. 32, pp. 3330–3332, 2007.

[15] F. Théberge, M. Châteauneuf, G. Roy, P. Mathieu, and J. Dubois, "Generation of tunable and broadband far-infrared laser pulses during two-color filamentation," *Phys. Rev. A*, vol. 81, p. 033821, 2010.

[16] P. B. Petersen and A. Tokmakoff, "Source for ultrafast continuum infrared and terahertz radiation," *Opt. Lett.*, vol. 35, pp. 1962–1964, 2010.

[17] Y. Nomura *et al.*, "Phase-stable sub-cycle mid-infrared conical emission from filamentation in gases," *Opt. Exp.*, vol. 20, pp. 24741–24747, 2012.

[18] P. Lassonde *et al.*, "Infrared generation by filamentation in air of a spectrally shaped laser beam," *Opt. Exp.*, vol. 19, pp. 14093–14098, 2011.

[19] M. D. Thomson, V. Blank, and H. G. Roskos, "Terahertz white-light pulses from an air plasma photo-induced by incommensurate two-color optical fields," *Opt. Exp.*, vol. 18, pp. 23173–23182, 2010.

[20] C. Calabrese, A. M. Stingel, L. Shen, and P. B. Petersen, "Ultrafast continuum mid-infrared spectroscopy: Probing the entire vibrational spectrum in a single laser shot with femtosecond time resolution," *Opt. Lett.*, vol. 37, pp. 2265–2267, 2012.

[21] Y. Nomura *et al.*, "Single-shot detection of mid-infrared spectra by chirped-pulse upconversion with four-wave difference frequency generation in gases," *Opt. Exp.*, vol. 21, pp. 18249–18254, 2013.

[22] A. M. Stingel, C. Calabrese, and P. B. Petersen, "Strong intermolecular vibrational coupling through cyclic hydrogen-bonded structures revealed by ultrafast continuum mid-IR spectroscopy," *J. Phys. Chem. B*, vol. 117, pp. 15714–15719, 2013.

[23] H. Shirai, T.-T. Yeh, Y. Nomura, C.-W. Luo, and T. Fuji , "Ultrabroadband mid-infrared pump-probe spectroscopy using chirped-pulse upconversion in gases," *Phys. Rev. Appl.*, vol. 3, no. 5, art. no. 051002, May 2015.

[24] T. Fuji and Y. Nomura, "Generation of phase-stable sub-cycle mid-infrared pulses from filamentation in nitrogen," *Appl. Sci.*, vol. 3, pp. 122–138, 2013.

[25] A. D. DiChiara *et al.*, "Scaling of high-order harmonic generation in the long wavelength limit of a strong laser field," *IEEE J. Sel. Topics Quantum Electron.*, vol. 18, no. 1, pp. 419–433, Jan./Feb. 2012.

[26] T. Popmintchev *et al.*, "Bright coherent ultrahigh harmonics in the KeV X-ray regime from mid-infrared femtosecond lasers," *Science*, vol. 336, pp. 1287–1291, 2012.

[27] Y. Nomura, H. Shirai, and T. Fuji, "Frequency-resolved optical gating capable of carrier-envelope phase determination," *Nature Commun.*, vol. 4, pp. 2820-1–2820-11, 2013.

[28] H. Shirai, Y. Nomura, and T. Fuji, "Real-time waveform characterization by using frequency-resolved optical gating capable of carrier-envelope phase determination," *IEEE Photon. J.*, vol. 6, no. 3, pp. 1–12, Jun. 2014.

[29] C. R. Baiz and K. J. Kubarych, "Ultrabroadband detection of a mid-IR continuum by chirped-pulse upconversion," *Opt. Lett.*, vol. 36, pp. 187–189, 2011.

[30] J. Dai, N. Karpowicz, and X. C. Zhang, "Coherent polarization control of terahertz waves generated from two-color laser-induced gas plasma," *Phys. Rev. Lett.*, vol. 103, p. 023001, 2009.

[31] L. Misoguti *et al.*, "Generation of broadband VUV light using third-order cascaded processes," *Phys. Rev. Lett.*, vol. 87, p. 013601, 2001.

[32] A. Couairon and A. Mysyrowicz, "Femtosecond filamentation in transparent media," *Phys. Rep.*, vol. 441, pp. 47–189, 2007.

[33] L. Bergé, S. Skupin, R. Nuter, J. Kasparian, and J. P. Wolf, "Ultrashort filaments of light in weakly ionized, optically transparent media," *Rep. Prog. Phys.*, vol. 70, pp. 1633–1713, 2007.

[34] J. Yao *et al.*, "Remote creation of coherent emissions in air with two-color ultrafast laser pulses," *New J. Phys.*, vol. 15, pp. 023046-1–023046-10, 2013.

[35] S. Linden, H. Giessen, and J. Kuhl, "XFROG—A new method for amplitude and phase characterization of weak ultrashort pulses," *Phys. Status Solidi B*, vol. 206, pp. 119–124, 1998.

[36] H. Shirai, C. Duchesne, Y. Furutani, and T. Fuji, "Attenuated total reflectance spectroscopy with chirped-pulse upconversion," *Opt. Exp.*, vol. 22, pp. 29 611–29 616, 2014.

[37] K. F. Lee, P. Nuernberger, A. Bonvalet, and M. Joffre, "Removing cross-phase modulation from midinfrared chirped-pulse upconversion spectra," *Opt. Exp.*, vol. 17, pp. 18738–18744, 2009.

[38] M. Kress, T. Löffler, S. Eden, M. Thomson, and H. G. Roskos, "Terahertz-pulse generation by photoionization of air with laser pulses composed of both fundamental and second-harmonic waves," *Opt. Lett.*, vol. 29, pp. 1120–1122, 2004.

[39] X. Xie, J. Dai, and X. C. Zhang, "Coherent control of THz wave generation in ambient air," *Phys. Rev. Lett.*, vol. 96, p. 075005, 2006.

[40] H. Zhong, N. Karpowicz, and X. C. Zhang, "Terahertz emission profile from laser-induced air plasma," *Appl. Phys. Lett.*, vol. 88, p. 261103, 2006.

[41] K.-Y. Kim, J. H. Glownia, A. J. Taylor, and G. Rodriguez, "Terahertz emission from ultrafast ionizing air in symmetry-broken laser fields," *Opt. Exp.*, vol. 15, pp. 4577–4584, 2007.

[42] K. Y. Kim, A. J. Taylor, J. H. Glownia, and G. Rodriguez, "Coherent control of terahertz supercontinuum generation in ultrafast laser-gas interactions," *Nature Photon.*, vol. 2, pp. 605–609, 2008.

[43] H. Wen and A. M. Lindenberg, "Coherent terahertz polarization control through manipulation of electron trajectories," *Phys. Rev. Lett.*, vol. 103, p. 023902, 2009.

[44] F. Blanchard *et al.*, "Improved terahertz two-color plasma sources pumped by high intensity laser beam," *Opt. Exp.*, vol. 17, pp. 6044–6052, 2009.

[45] Y. Liu, A. Houard, M. Durand, B. Prade, and A. Mysyrowicz, "Maker fringes in the terahertz radiation produced by a 2-color laser field in air," *Opt. Exp.*, vol. 17, pp. 11 480–11 485, 2009.

[46] Y. S. You, T. I. Oh, and K. Y. Kim, "Off-axis phase-matched terahertz emission from two-color laser-induced plasma filaments," *Phys. Rev. Lett.*, vol. 109, p. 183902, 2012.

[47] G. Gallot and D. Grischkowsky, "Electro-optic detection of terahertz radiation," *J. Opt. Soc. Amer. B*, vol. 16, pp. 1204–1212, 1999.

[48] G. C. Bjorklund, "Effects of focusing on third-order nonlinear processes in isotropic media," *IEEE J. Quantum Electron.*, vol. 11, no. 6, pp. 287–296, Jun. 1975.

[49] A. Voronin, Y. Nomura, H. Shirai, T. Fuji, and A. Zheltikov, "Half-cycle pulses in the mid-infrared from a two-color laser-induced filament," *Appl. Phys. B*, vol. 117, pp. 611–619, 2014.

[50] P. Klarskov, A. C. Strikwerda, K. Iwaszczuk, and P. U. Jepsen, "Experimental three-dimensional beam profiling and modeling of a terahertz beam generated from a two-color air plasma," *New J. Phys.*, vol. 15, pp. 075012-1–075012-13, 2013.

[51] G. Cerullo, A. Baltuška, O. D. Muecke, and C. Vozzi, "Few-optical-cycle light pulses with passive carrier-envelope phase stabilization," *Laser Photon. Rev.*, vol. 5, pp. 323–351, 2011.

[52] T. Fuji *et al.*, "Parametric amplification of few-cycle carrier-envelope phase-stable pulses at 2.1 μm," *Opt. Lett.*, vol. 31, pp. 1103–1105, 2006.

[53] L. Bergé, C. L. Soulez, C. Koehler, and S. Skupin, "Role of the carrier-envelope phase in laser filamentation," *Appl. Phys. B*, vol. 103, pp. 563–570, 2011.

[54] C. Manzoni, M. Först, H. Ehrke, and A. Cavalleri, "Single-shot detection and direct control of carrier phase drift of midinfrared pulses," *Opt. Lett.*, vol. 35, pp. 757–759, 2010.

[55] D. J. Kane and R. Trebino, "Single-shot measurement of the intensity and phase of an arbitray ultrashort pulse by using frequency-resolved optical gating," *Opt. Lett.*, vol. 18, pp. 823–825, 1993.

[56] R. Trebino, *Frequency-Resolved Optical Gating: The Measurement of Ultrashort Laser Pulses*. Norwell, MA, USA: Kluwer, 2000.

[57] Q. Wu and X.-C. Zhang, "Free-space electrooptic sampling of teraherz beams," *Appl. Phys. Lett.*, vol. 67, pp. 3523–3525, 1995.

[58] A. A. Lanin, A. B. Fedotov, and A. M. Zheltikov, "Ultrabroadband XFROG of few-cycle mid-infrared pulses by four-wave mixing in a gas," *J. Opt. Soc. Amer. B*, vol. 31, pp. 1901–1905, 2014.

[59] N. Karpowicz *et al.*, "Coherent heterodyne time-domain spectrometry covering the entire 'terahertz gap'" *Appl. Phys. Lett.*, vol. 92, p. 011131, 2008.

[60] R. Kanya and Y. Ohshima, "Pendular-state spectroscopy of the S_1 S_0 electronic transition of 9-cyanoanthracene," *J. Chem. Phys.*, vol. 121, pp. 9489–9497, 2004.

[61] W. H. Press, W. T. Vetterling, S. A. Teukolsky, and B. P. Flannery, *Numerical Recipes in C++: The Art of Scientific Computing*, 2nd ed. New York, NY, USA: Cambridge Univ. Press, 2002.

[62] Z. Wang, E. Zeek, R. Trebino, and P. Kvam, "Beyond error bars: Understanding uncertainty in ultrashort-pulse frequency-resolved-optical-gating measurements in the presence of ambiguity," *Opt. Exp.*, vol. 11, pp. 3518–3527, 2003.

[63] Z. Wang, E. Zeek, R. Trebino, and P. Kvam, "Determining error bars in measurements of ultrashort laser pulses," *J. Opt. Soc. Amer. B*, vol. 20, pp. 2400–2405, 2003.

[64] A. Sell, A. Leitenstorfer, and R. Huber, "Phase-locked generation and field-resolved detection of widely tunable terahertz pulses with amplitudes exceeding 100 MV/cm," *Opt. Lett.*, vol. 33, pp. 2767–2769, 2008.

[65] Y. Nomura, Y.-T. Wang, A. Yabushita, C.-W. Luo, and T. Fuji, "Controlling the carrier-envelope phase of single-cycle mid-infrared pulses with two-color filamentation," *Opt. Lett.*, vol. 40, pp. 423–426, 2015.

[66] T. Fuji, Y. Nomura, Y.-T. Wang, A. Yabushita, and C. W. Luo, "Carrier-envelope phase of single-cycle pulses generated through two-color laser filamentation," presented at the 19th Int. Conf. Ultrafast Phenomena, Opt. Soc. Amer., Okinawa Japan, 2014, Paper 08.Tue.D.1.

[67] M. Kress *et al.*, "Determination of the carrier-envelope phase of few-cycle laser pulses with terahertz-emission spectroscopy," *Nature Phys.*, vol. 2, pp. 327–331, 2006.

[68] M. D. Thomson, M. Kress, T. Loeffler, and H. G. Roskos, "Broadband THz emission from gas plasmas induced by femtosecond optical pulses: From fundamentals to applications," *Laser Photon. Rev.*, vol. 1, pp. 349–368, 2007.

[69] I. Babushkin, S. Skupin, and J. Herrmann, "Generation of terahertz radiation from ionizing two-color laser pulses in Ar filled metallic hollow waveguides," *Opt. Exp.*, vol. 18, pp. 9658–9663, 2010.

[70] I. Babushkin *et al.*, "Tailoring terahertz radiation by controlling tunnel photoionization events in gases," *New J. Phys.*, vol. 13, pp. 123029-1–123029-12, 2011.

[71] M. Li *et al.*, "Verification of the physical mechanism of THz generation by dual-color ultrashort laser pulses," *Appl. Phys. Lett.*, vol. 101, p. 161104, 2012.

[72] R. W. Boyd, *Nonlinear Optics*, 3rd ed. San Diego, CA, USA: Academic, 2008.

Yutaka Nomura was born in Matsudo, Japan, in 1979. He received the B.S. and M.S. degrees in physics from the University of Tokyo, Tokyo, Japan, in 2002 and 2004, respectively, and the Ph.D. degree in physics from the Ludwig Maximilian University of Munich, Munich, Germany, in 2008.

In 2008, he was a Postdoctoral Researcher with the Max Planck Institute of Quantum Optics, Garching, Germany. From 2008 to 2010, he was a Project Researcher with the Institute for Solid State Physics, University of Tokyo, Kashiwa, Japan. In 2010, he was a JSPS Research Fellow. Since 2010, he has been an Assistant Professor at the Institute for Molecular Science, Okazaki, Japan. His research interests include development of ultrafast fiber laser systems, nonlinear optics, and ultrafast spectroscopy.

Dr. Nomura is a Member of the Optical Society of America, the Japan Society of Applied Physics, the Physical Society of Japan, and the Laser Society of Japan.

Takao Fuji was born in Kyoto, Japan, in 1972. He received the B.S., M.S., and Ph.D. degrees from the University of Tsukuba, Tsukuba, Japan, in 1994, 1996, and 1999, respectively, all in engineering.

Starting in 1999, he was a Research Associate with the University of Tokyo, Tokyo, Japan. In 2002, with the support from the JSPS Postdoctoral Fellowships for Research Abroad, he was a Guest Researcher with the Vienna University of Technology. In 2004, he was a Postdoctoral Researcher with the Max Planck Institute of Quantum Optics, Garching, Germany. In 2006, he was a Research Scientist with RIKEN, Wako, Japan. Since 2010, he has been an Associate Professor at the Institute for Molecular Science, Okazaki, Japan. His research interests include development of ultrashort pulse lasers, nonlinear optics, and ultrafast spectroscopy.

Dr. Fuji is a Member of the Optical Society of America, the Japan Society for Molecular Science, the Physical Society of Japan, and the Laser Society of Japan. He received the Encouragement Award of the Optical Society of Japan in 1999 and the Kondo Award of Osaka University in 2008.

Hideto Shirai was born in Takamatsu, Japan, in 1983. He received the B.S., M.S., and Ph.D. degrees from Kagawa University, Takamatsu, Japan, in 2008, 2010, and 2013, respectively, all in engineering.

Since 2013, he has been a Postdoctoral Researcher, which is named as an IMS Fellow at the Institute for Molecular Science, Okazaki, Japan. His research interests include nonlinear optics and ultrafast spectroscopy.

Dr. Shirai is a Member of the Physical Society of Japan and the Japan Society of Applied Physics,